Article

Long-Lived Spin-Correlated Pairs Generated by Photolysis of Naphthalene Occluded in Non-Brønsted Acidic ZSM-5 Zeolites

Alain Moissette, Sverine Marquis, David Cornu, Herv Vezin, and Claude Brmard

J. Am. Chem. Soc., **2005**, 127 (44), 15417-15428• DOI: 10.1021/ja0518225 • Publication Date (Web): 13 October 2005

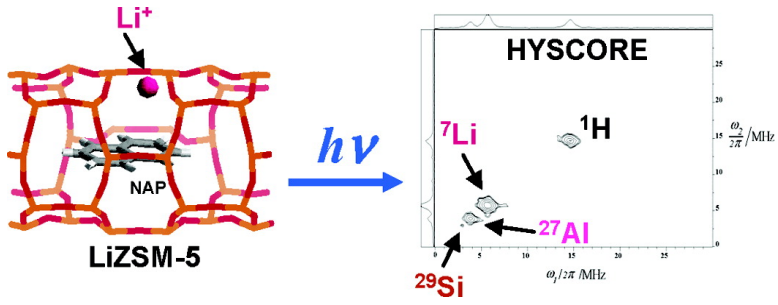

More About This Article

Additional resources and features associated with this article are available within the HTML version:

- Supporting Information
- Links to the 2 articles that cite this article, as of the time of this article download
- Access to high resolution figures
- Links to articles and content related to this article
- Copyright permission to reproduce figures and/or text from this article

View the Full Text HTML

J|A|C|S
ARTICLES
Published on Web 10/13/2005

Long-Lived Spin-Correlated Pairs Generated by Photolysis of Naphthalene Occluded in Non-Brønsted Acidic ZSM-5 Zeolites

Alain Moissette,*,† Séverine Marquis,† David Cornu,† Hervé Vezin,‡ and Claude Brémard†

Contribution from the Laboratoire de Spectrochimie Infrarouge et Raman UMR-CNRS 8516, Centre d' Etudes et de Recherches Lasers et Applications, Bât. C5 Université des Sciences et Technologies de Lille, 59655 Villeneuve d'Ascq Cedex, France, and Laboratoire de Chimie Organique et Macromoléculaire UMR-CNRS 8009, Bât. C3 Université des Sciences et Technologies de Lille, 59655 Villeneuve d'Ascq Cedex, France.

Received March 22, 2005; E-mail: alain.moissette@univ-lille1.fr

Abstract: Long-lived spin-correlated pairs were generated by laser irradiation of naphthalene (NAP) occluded as intact molecule within non-Brønsted acidic M_nZSM-5 zeolites with $M_nSiO_2)_{96-n}(AlO_2)_n$ formula per unit cell. The laser UV photoionization generates primary $NAP^{\bullet+}$−electron pair as a fast phenomenon. These charge carriers exhibit lifetimes that extend over less than 1 h at room temperature and disappear according to two parallel competitive ways: direct charge recombination and electron transfer. This subsequent electron transfer takes place between the electron-deficient radical cation ($NAP^{\bullet+}$) and the electron-donor oxygen atom of zeolite framework. The aluminum rich M_nZSM-5 zeolites ($n = 3.4$, 6.6) hinder efficiently the charge recombination and promote the electron transfer to generate a very long electron−hole pair which exceeds several weeks at room temperature in $NAP@Li_{6.6}ZSM$-5. The electron−hole pair exhibits broad visible absorption bands at 482 and 525 nm. The electron−hole distance, 1.3 nm, was deduced from the dipolar interaction term (D) value. The spin density of trapped electron appears spread over ^{27}Al, ^{29}Si, ^{7}Li, and ^{1}H nuclei as deduced by two-dimensional approach of hyperfine sublevel correlation (HYSCORE). The very low recombination rate by tunneling effect was found to be in agreement with the very low value ($J \approx 0$) of the magnetic exchange. The combined effects of tight fit between NAP size and straight-channel dimension, the high aluminum content of the framework, and the highly polarizing cation Li^+ trapped efficiently the ejected electron in the conduction band and the hole in the valence band of the porous materials.

Introduction

Recent studies on photoinduced electron-transfer reactions have shown that the formation and the subsequent reactions of spin correlated pairs are the crucial steps in several applications of the light energy storage via electron transfer.[1] In solution, photogenerated compact ion pairs have lifetimes well below microseconds, whereas solvent-separated ion pairs can live orders of magnitude longer. In contrast, in the void space of porous materials, photogenerated ion pairs can exhibit a lifetime increased by a factor of 10^5-10^6 at room temperature compared to that measured in solution.[2]

There have been a considerable number of papers confirming that radical cations generated by photoionization of occluded guests become stabilized within zeolites and they are long-lived, decaying in several seconds or more.[3] Unfortunately, there is limited experimental information to identify the fate of the ejected electron.[3] The whereabouts of ejected electrons within the inorganic supports remain difficult to evaluate. It was previously reported that zeolite matrixes can contribute through three different ways to the electron-transfer reactions: (i) inert medium, (ii) electron acceptor, and (iii) electron donor.[4]

Studies on the remarkable effects on different photophysical and photochemical processes of aromatic hydrocarbons in different media including porous materials such as zeolites have been reported.[2−6] Naphthalene (NAP) has been very often the probe molecule of choice because its photophysics and photochemistry in solvents, micelles, glasses, and faujasitic zeolites are well documented.[7−12] Recently, we have reported the

† Laboratoire de Spectrochimie Infrarouge et Raman UMR-CNRS 8516, Centre d' Etudes et de Recherches Lasers et Applications, Bât. C5 Université des Sciences et Technologies de Lille.

‡ Laboratoire de Chimie Organique et Macromoléculaire UMR-CNRS 8009, Bât. C3 Université des Sciences et Technologies de Lille.

(1) Borja, M.; Dutta, P. K. *Nature* **1993**, *362*, 43−45.
(2) Ramamurthy, V.; Lakshminarasimhan, P.; Grey, C. P.; Johnston, L. J. *Chem. Commun.* **1998**, 2411−2424.
(3) Garcia, H.; Roth, H. D. *Chem. Rev.* **2002**, *102*, 3947−4007.
(4) Hashimoto, S. *J. Photochem. Photobiol., C* **2003**, *4*, 19−49.
(5) Werst, D. W.; Han, P.; Trifunac, A. D. *Radiat. Phys. Chem*. **1998**, *51*, 255−262.
(6) Scaiano, J. C.; Garcia, H. *Acc. Chem. Res.* **1999**, *32*, 783−793.
(7) Nakabayashi, T.; Kamo S.; Sakuragi H.; Nishi N. *J. Phys. Chem. A* **2001**, *105*, 8605−8614.
(8) Hubig, S. M. *J. Phys. Chem*. **1992**, *96*, 2903−2909.
(9) Iu, K−K.; Liu X.; Thomas J. K. *J. Photochem. Photobiol., A* **1994**, *79*, 103−107.
(10) Hashimoto, S.; Mutoh, T.; Fukumura, H.; Masuhara, H. *J. Chem. Soc., Faraday Trans.* **1996**, *92*, 3653−3660.
(11) Erickson, R.; Benetis, N. P.; Lund, A.; Lindgren, M.*J. Phys. Chem.* **1997**, *101*, 2390−2396.

10.1021/ja0518225 CCC: $30.25

spontaneous ionization of NAP and subsequent long-lived electron−hole pair formation after the mere exposure of solid NAP to dehydrated Brønsted acidic H_nZSM-5.[13] Particularly, the high aluminum content and the acidity combined with the tight fit between the NAP shape and the narrow pore size of ZSM-5 zeolites were found to be responsible for spontaneous and durable ionization.[13]

In this article, we report the study of the fate of the radical cation−electron pair generated by laser photolysis of naphthalene occluded as an intact molecule in non-Brønsted acidic M_nZSM-5 zeolites with $M_n(AlO_2)_n(SiO_2)_{96-n}$ unit cell formula (n = 0.0, 3.0, 3.4, 6.6; M = Li^+, Na^+, K^+, Rb^+, Cs^+). The charge recombination and subsequent electron transfer were explored as functions of the aluminum content of the framework (n) of the nature of the counterbalancing cation (M^+) using diffuse reflectance UV−visible absorption spectroscopy (DRUVv) and continuous wave electron paramagnetic resonance (CW-EPR). The dipolar interactions between the two spins of long-lived spin-correlated pairs were studied to provide distance between the two spins. The X-band two-dimensional hyperfine sublevel correlation spectra (2D-HYSCORE) provided a detailed description of the microenvironment of the unpaired electrons of the very long-lived electron−hole pairs stabilized in aluminum-rich ZSM-5 zeolites.

Experimental Section

1. Materials. As-synthesized ZSM-5 samples (Si/Al = 13.5, 27, average particle size 1 μm) were obtained according to the template procedure in alkaline medium from VAW aluminum (Schwandorf, Germany). Crystals of silicalite-1 (Si/Al > 1000) and Al−ZSM-5 (Si/Al ≈ 31, average particle size 2 μm) were synthesized in high purity according to the fluoride medium procedure in the "Laboratoire des Matériaux Minéraux", UMR-CNRS 7016, Mulhouse, France. The as-synthesized ZSM-5 zeolites were calcined under air to evacuate the template. The extraframework cations were completely exchanged by Li^+, Na^+, K^+, Rb^+, Cs^+.[5,14] All the bare zeolite samples were dehydrated by a calcination procedure up to 773 K under argon. The chemical analyses, powder XRD patterns, ^{29}Si, ^{27}Al MAS NMR, IR, Raman, DRUVv, and EPR spectra of bare ZSM-5 zeolites were found to be characteristic of well-crystallized porous compounds with the following formula per unit cell: $M_n(AlO_2)_n(SiO_2)_{96-n}$ (n = 0.0, 3.0, 3.4, 6.6; M^+= Li^+, Na^+, K^+, Rb^+, Cs^+). Particularly, no evidence was found for Brønsted and true Lewis acidic sites using IR absorption spectrometry and pyridine absorption. However, the ^{27}Al NMR spectra of hydrated $M_{6.6}ZSM-5$ (Si/Al = 13.5) samples provide evidence of small amounts of extraframework hexacoordinated Al species. Naphthalene (NAP, $C_{10}H_8$, Merck-Schuchardt) was purified by sublimation. Pure air and dry Ar gas was used.

2. Sorption of NAP in M_nZSM-5. Weighed amounts (~1.4 g) of powdered hydrated zeolite $M_n(AlO_2)_n(SiO_2)_{96-n}$ were introduced into an evacuable, heatable silica cell. The sample was heated to 773 K under Ar. Then, the sample was cooled to room temperature under dry argon. Weighted amounts of NAP corresponding to 1 molecule per zeolite unit cell (UC) were introduced in the dark into the cell, and the powders were shaken. The powders were transferred under dry argon in a quartz glass Suprasil cell for FT-Raman and DRUVv experiments or in cylindrical EPR quartz tube and sealed. The loaded $NAP@M_n(AlO_2)_n(SiO_2)_{96-n}$ samples were studied and irradiated after complete sorption and equilibration.

3. Molecular Modeling. The molecular modeling of the NAP-preferred sorption sites in $M_n(AlO_2)_n(SiO_2)_{96-n}$ zeolites were performed on a Silicon Graphics workstation using Cerius2 (version 3.8) package from Molecular Simulations Incorporation. The zeolite structural parameters and partial atomic charges of $M_n(AlO_2)_n(SiO_2)_{96-n}$ (n = 0, 4) were taken from previous works and introduced in the crystal builder module of Cerius2.[15,16] The structural parameters and set of partial atomic charges of NAP were derived from previous structural and theoretical works.[17−19] The nonbonding Lennard-Jones (L-J) force field values were taken from previous works and introduced in the open force field module of Cerius2.[16,20] In the Monte Carlo (MC) simulations, the Si, Al, O, and M^+ positions were fixed in the simulation box. The simulation box of ZSM-5 was a supercell that consists of 2 × 2 × 4 orthorhombic cells. Periodic boundary conditions were applied in all directions. The NAP structure was taken to be rigid. The MC simulations at 1 NAP/UC loading were carried out at 300 K using the conventional Metropolis algorithm taking into account the nonbonding interactions (E_{ZS}) between the O and M^+ atoms of zeolite and the C and H atoms of NAP as well as the nonbonding interactions (E_{SS}) between NAP. The interactions inside the zeolite were modeled by L-J and Coulombic forces.

$$E_{ZS} + E_{SS} = \sum_{ij} A_{\alpha\beta}/r_{ij}^{12} - B_{\alpha\beta}/r_{ij}^{6} + q_i q_j/r_{ij} \quad (1)$$

A cutoff radius of 0.9 nm was applied to the L-J interactions. The long-range electrostatic interactions were calculated using the Ewald summation technique. The simulation takes a number of steps to equilibrate from its original random position. For accurate statistical results, the steps made prior to equilibration have been excluded of the analysis. One typical MC run took 1 500 000 steps. From each sorption trajectory, a histogram of the energy distribution for each sorbate was generated. In a so-called mass-cloud analysis the center of mass of each sorbate in each configuration was displayed as a dot in the model space. In the molecular mechanics (MM) simulations the time-consuming Ewald summation has not been performed. The zeolite framework was taken to be rigid, and the extraframework cations M^+ and rigid NAP were taken to be mobile.

$$E_{ZS} + E_{SS} + E_{ZM} + E_{MM} = \sum_{ij} A_{\alpha\beta}/r_{ij}^{12} - B_{\alpha\beta}/r_{ij}^{6} + q_i q_j/r_{ij} \quad (2)$$

The electrostatic and (L-J) interaction cutoffs are defined by two parameters: the spline-on and the spline-off distances. Within these ranges the nonbonded interaction energy is attenuated by a spline function. Beyond the spline-off distance nonbonded interactions were ignored. The spline-on and spline-off distances were taken to be 1.5 and 3 nm for both the electrostatic and (L-J) interactions. The energy minimization of nonbonding sorbate−zeolite energy was performed using the conjugate gradient minimization procedure.

4. Photolysis. The photolysis of the bare $M_n(AlO_2)_n(SiO_2)_{96-n}$ and loaded $NAP@M_n(AlO_2)_n(SiO_2)_{96-n}$ samples contained under Ar in Suprasil cuvettes or quartz tubes was carried out at room temperature during 15 s with a pulsed Nd:YAG laser (10 ns, 10 Hz) operating at 266-nm wavelength with 30 mJ/cm^2 power. The UV−visible diffuse reflectance and CW-EPR spectra were recorded at room temperature before and after the laser irradiation period as a function of time over several days.

(12) Marquez, F.; Zicovich-Wilson, C. M.; Corma, A.; Palomares, E.; Garcia, H. *J. Phys. Chem.* **2001**, *105*, 9973−9979.
(13) Moissette, A.; Vezin, H.; Gener, I.; Brémard, C. *J. Phys. Chem. B* **2003**, *107*, 8935−8945.
(14) Brémard, C.; Lemaire, M. *J. Phys. Chem.* **1993**, *97*, 9695−9702.
(15) Olson, D. H.; Khosrovani, N.; Peters, A. W.; Toby, B. H. *J. Phys. Chem. B* **2000**, *104*, 4844−4848.
(16) Beerdsen, E.; Dubbeldam, D.; Smit, B.; Vlugt, T. J. H.; Calero, S. *J. Phys. Chem.* **2003**, *107*, 12088−12096.
(17) Baehtz, C.; Fuess, H. *Phys. Chem. Chem. Phys.* **2002**, *4*, 4543−4548.
(18) Oddershede, J.; Larsen, S. *J. Phys. Chem. B* **2004**, *108*, 1057−1063.
(19) Morin, C.; Simon, D.; Sautet, P. *J. Phys. Chem. B* **2004**, *188*, 12084−12091.
(20) Gener, I.; Buntinx, G.; Brémard, C. *Microporous Mesoporous Mater.* **2000**, *41*, 253−268.

5. Instrumentation. Diffuse Reflectance UV−Visible Absorption. The UV−visible absorption spectra of the samples were recorded between 200 and 800 nm using a Cary 3 spectrometer. The instrument was equipped with an integrating sphere to study the powdered zeolite samples through diffuse reflectance; the corresponding bare zeolite was used as the reference. The DRUVv spectra were plotted as the Kubelka−Munk function:

$$F(R) = (1 - R)^2/2\mathrm{R} = K/S \tag{3}$$

where R represents the ratio of the diffuse reflectance of the loaded zeolite to that of the dehydrated neat zeolite, K designates an absorption coefficient proportional to the concentration C of the chromophore and S the scattering coefficient of the powder. $\boldsymbol{F}(\lambda, t)$ were registered as function of λ (wavelength) at several t (time).

Raman Scattering Spectroscopy. A Bruker IFS 88 instrument was used as a near-IR FT-Raman spectrometer with a CW Nd:YAG laser at 1064 nm as excitation source. A laser power of 100−200 mW was used. The spectra (3500−150 cm^{-1}) were recorded with a resolution of 2 cm^{-1} using 600 scans. The Opus Bruker software was used for spectral acquisition, data treatment, and plotting. The vibrational properties of NAP are well documented. The isolated NAP molecule belongs to D_{2h} molecular symmetry group and has 9 A_g + 3 B_{1g} + 4 B_{2g} + 8 B_{3g} + 8 B_{1u} + 8 B_{2u} + 4 B_{3u} + 4 A_u fundamental vibrational modes with A_g, B_{1g}, B_{2g}, B_{3g} Raman active.

IR Absorption Spectrometry. In situ FTIR spectra were recorded in the region 4000−400 cm^{-1} on a Nicolet 730 spectrometer, using a homemade cell and thin self-supported wafers (8−10 mg/cm^2). The cell was connected to an evacuation gas flow system, which allowed thermal treatment up to 900 K. The bare zeolite wafers were first calcined overnight in O_2 at 773 K and then evacuated under vacuum for 1 h. The spectra were recorded before, after pyridine adsorption, and after evacuation under vacuum. The Brønsted acidic sites of ZSM-5 protonate pyridine, forming the pyridinium ion, which has a characteristic band at 1545 cm^{-1}; Lewis acidic aluminum site giving rise to a vibrational band at 1465 cm^{-1}.

X-band EPR Spectroscopy. The CW X-band EPR spectra (dχ"/dB) were recorded between 300 and 4.2 K on a Bruker ELEXYS 580-FT spectrometer using an Oxford helium cryostat.

The pulsed EPR experiments were performed on a Bruker ELEXYS 580-FT spectrometer at 300 and 4.2 K. The one-dimensional two pulses ESEEM experiment $\pi/2-\tau-\pi-\tau$ echo was achieved with 16 and 32 ns pulses by recording the echo intensity as a function of time τ. The 2D-HYSCORE measurements were carried out with the four pulse sequence $\pi/2-\tau-\pi/2-t_1-\pi-t_2-\pi/2-\tau$ echo, and a four-step phase cycle where the echo is measured as a function of t_1 and t_2; t_1 and t_2 were incremented in steps of 16 ns from their initial value. The pulse lengths of the $\pi/2$ and π pulses in these experiments were 12 and 32 ns, respectively. The 2D-HYSCORE experiments were recorded with two different delay τ values of 88 and 156 ns, respectively. Prior to Fourier transformation of the HYSCORE data the background decay was removed by a polynomial fit and apodized with a Hamming function.

6. Data Processing, Kinetic Calculations, and Theoretical Background. The data processing of DRUVv spectral set $\boldsymbol{F}(\lambda,t)$ was carried out using the SIMPLISMA (SIMPle-to-use interactive self-modeling mixture analysis) approach. This method was applied to extract pure UV absorption spectra (P) and respective concentration (C) from huge spectral data recorded as a function of time after the photolysis without any prior information.

$$\boldsymbol{F}(\lambda,t) = \boldsymbol{C}(t) \times \mathbf{P}(\lambda)^{\boldsymbol{T}} + \mathbf{E} \tag{4}$$

$\boldsymbol{F}(\lambda, t)$ represents the original data matrix with spectra in rows, $\boldsymbol{C}(t)$ represents the "concentration" matrix, obtained by using the columns of C. $\boldsymbol{P}(\lambda)^{\boldsymbol{T}}$ represents the transpose of $\boldsymbol{P}(\lambda)$, and $\boldsymbol{E}$ represents the residual error. $\boldsymbol{P}(\lambda)$ was calculated by standard matrix algebra. The SIMPLISMA algorithm and matrix calculations are detailed elsewhere.[21,22] The relative root sum of squares coefficient calculates residuals and represents the difference between the calculated and experimental data.

The concentrations functions $C(t)$ were accurately fitted using the Albery function. This Gaussian distribution kinetic model is based on dispersion of the first-order rate constants $k = \bar{k}\exp(\gamma x)$; $\bar{k}$ is the average rate constant, and γ is the width of the distribution. The decay kinetics fitting was carried out by using the Microcal Origin software.[23]

According to the model, concentration decays can be represented by eq 5:

$$C(t) = C/C_0 = \frac{\int_{-\infty}^{+\infty} \exp(-x^2)\exp(-\bar{k}t\exp(\gamma x))\mathrm{d}x}{\int_{-\infty}^{+\infty} \exp(-x^2)\mathrm{d}x} \tag{5}$$

where $\int_{-\infty}^{+\infty} \exp(-x^2)\mathrm{d}x = \sqrt{\pi}$ and $C(t)$ is the normalized concentration. If $\gamma = 0$ (no dispersion), the eq 5 is reduced to first-order kinetics: $C(t) = \exp(-kt)$. A simple numerical procedure for integrating the numerator in eq 5 using only $\bar{k}$ and γ parameters is detailed in the appendix of the original publication.[23]

The double integrated $\boldsymbol{n}$ values of overall CW-EPR signals (dχ"/dB) recorded as a function of time after the photolysis were analyzed using a model in which the charge recombination mechanism consists of a tunneling process.[24,25] The recombination rate can be written as

$$\nu(r) = \nu_0 \exp(-2r/a) \tag{6}$$

where $\nu(r)$ describes the recombination rate of any electron and hole that are separated by a distance r; ν_0 is a recombination constant that may be interpreted as an attempt to recombine frequency. The parameter a describes an effective localization radius that is assumed to be equivalent for the electron and hole. From eq 6 it follows that after some time t, spatially close carriers will have recombined, thus leaving carriers with larger distances behind. Therefore, by recombination of the closest pairs, the nearest-neighbor distance $r(t)$ increases and can be written as

$$r(t) = a/2\ln(t\nu_0) \tag{7}$$

Now, assuming that the photoexcitation is turned off at some time $t_0 = 0$ at a charge carrier concentration n_0 and taking into account a time period $t_1 - t_0$, in which geminate recombination is present, it can be shown that for times larger than t_1 the remaining concentration of charge carriers $n(t)$ could be written as

$$n(r) = \frac{n_1}{1 + 4\pi/3[n_1(r^3 - r_1^3)]} \tag{8}$$

where the time dependence is contained in $r = r(t)$ given by eq 7 with $t > t_1$. $r(t)$ described the increase of the nearest neighbor distance among the remaining electron−hole pairs, $r_1 = r(t_1)$ described the nearest-neighbor electron−hole distance at t_1. n_1 is the charge carrier concentration at t_1. After very long times, i.e., at large r, one obtains $n(r) = [4\pi/3(r^3)]^{-1}$.

(21) Windig, W.; Guilment, J. *Anal. Chem.* **1991**, *63*, 1425−1432.
(22) Windig, W.; Antalek, B.; Lippert, J. L.; Batonneau, Y.; Brémard, C. *Anal. Chem.* **2002**, *74*, 1371−1379.
(23) Albery W. J.; Bartlett P. N.; Paul Wilde C.; Darwent J. R. *J. Am. Chem. Soc.* **1985**, *107*, 1854−1858.
(24) Shklovskii, B. I.; Fritzsche, H.; Baranovskii, S. D. *Phys. Rev. B* **1989**, *62*, 2989−2992. (25) Schultz, N. A.; Scharber, M. C.; Bradec, C. J.; Sariciftci, N. S. *Phys. Rev. B* **2000**, *64*, 245210−245217.
(25) Schultz, N. A.; Scharber, M. C.; Bradec, C. J.; Sariciftci, N. S. *Phys. Rev. B* **2000**, *64*, 245210−245217.

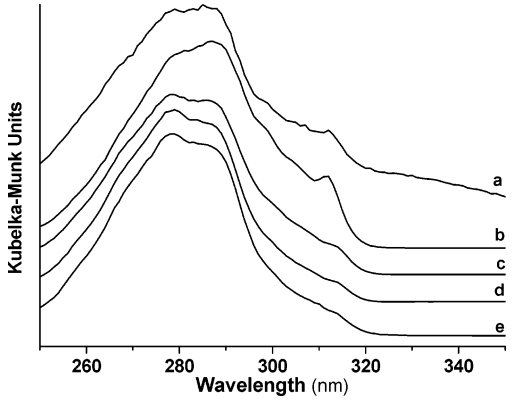

Figure 1. Room-temperature diffuse reflectance UV−vis absorption (DRUVv) spectra of naphthalene occluded within $M_{6.6}$ZSM-5 zeolites with 1 NAP/UC loading. M = (a) Li^+, (b) Na^+, (c) K^+, (d) Rb^+, (e) Cs^+. The spectra have been plotted as the Kubelka−Munk function.

Results

1. Diffuse Reflectance UV−Visible Absorption and Raman Scattering of NAP Occluded in M_nZSM-5 Zeolites. When a calculated quantity of solid NAP was exposed to dehydrated M_nZSM-5 crystals in the dark and under argon, the powdered samples remain white. The NAP loading used in the present work corresponds to 1 NAP per ZSM-5 unit cell. The inter- and intracrystalline migration of NAP was observable by means of conventional diffuse reflectance UV−visible absorption spectroscopy (DRUVv). The spectra were found to present marked analogy with spectra previously reported for NAP included within ferrierite, SSZ25 and ZSM-48 zeolites.[12] The three characteristic weak bands observed at 264, 270, and 285 nm for powdered solid NAP dispersed in the ZSM-5 zeolite powders evolved slowly to intense absorptions with wavelength shifts and relative intensity changes. The spectral evolution appeared to be complete several weeks after mixing. The rate of the spectral changes was found to depend on the size and number of extraframework cations. Gentle warming of the samples was found to facilitate the migration and the sorption. NAP and other polyaromatics are safely assumed to go into the large cavities of faujasite zeolites but scarcely go into the narrow channels of ZSM-5.[4,6] However, it was demonstrated recently that anthracene molecules penetrate slowly the channels of ZSM-5, while anthracene with bulky substituents were found to be blocked in the opening pore of the channels.[26] The DRUVv resulting spectra recorded after complete sorption for M = Cs^+, Rb^+, K^+ were found to exhibit four absorption bands at 265, 278, 287, and 316 nm with analogous relative intensities, while spectra recorded for Na^+ and Li^+ were found to show different relative intensities and a more prominent band at 313 nm (Figure 1). No band corresponding to radical cation $NAP^{\bullet+}$ was observed taking into account the different experimental conditions used (thermal treatment, Ar or O_2 atmosphere). The near-IR-FT Raman spectra recorded immediately after the NAP and zeolite powders mixing exhibit the spectral characteristics of NAP in the solid state (Figure 2, spectrum b). The characteristic Raman bands of solid NAP evolved slowly to Raman bands with some wavelength shifts and some relative intensity changes. The spectral evolution appeared to be complete several weeks after mixing. The resulting spectrum recorded for the NAP−silicalite-1 ($n = 0$) mixture after 1 month of contact is compared (1350−1600 cm^{-1}) with NAP spectra recorded in the bulk solid state and in solution in Figure 2. The spectra recorded for NAP−Na_nZSM-5 mixtures ($n = 3.4, 6.6$) were compared with that of NAP−silicalite-1 in Figure 3, while all the spectra recorded for NAP occluded in $M_{6.6}$ZSM-5 (M = Li^+, Na^+, K^+, Rb^+, Cs^+) were exhibited in Figure 4. The isolated NAP molecule belongs to D_{2h} molecular symmetry group and has 9 A_g + 3 B_{1g} + 4 B_{2g} + 8 B_{3g} + 8 B_{1u} + 8 B_{2u} + 4 B_{3u} + 4 A_u fundamental vibrational modes with A_g, B_{1g}, B_{2g}, B_{3g} Raman active. The bands observed around 3062 cm^{-1} in the bulk solid state are derived from the 2 A_g + 2 B_{3g} modes of the NAP molecule and are assigned to in-plane C−H stretching bonds. The bands observed at 1576 (medium, m), 1463 (m), 1444 (weak, w) and 1381 cm^{-1} (strong, s) for solid NAP are shown in Figure 2. These bands are derived from NAP molecular modes and are observed with analogous intensities at 1577 (A_g, m), 1461 (A_g, m), 1442 (B_{3g}, vw) and 1379 cm^{-1} (A_g, s). They are assigned to C−C stretches and ring planar deformations. [27]

The entrapment of NAP in the pores of silicalite-1 induced some wavenumber shifts of the corresponding bands from

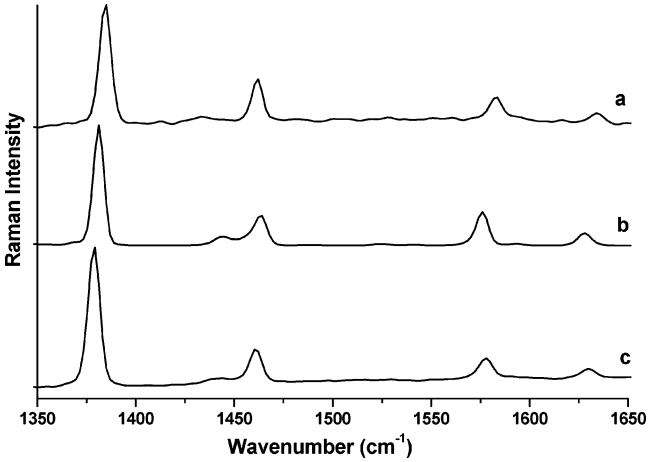

Figure 2. Room-temperature FT-Raman spectra recorded with 1064 nm laser exciting line. (a) NAP occluded within silicalite-1, (b) NAP as powdered solid, (c) NAP in chloroform solution.

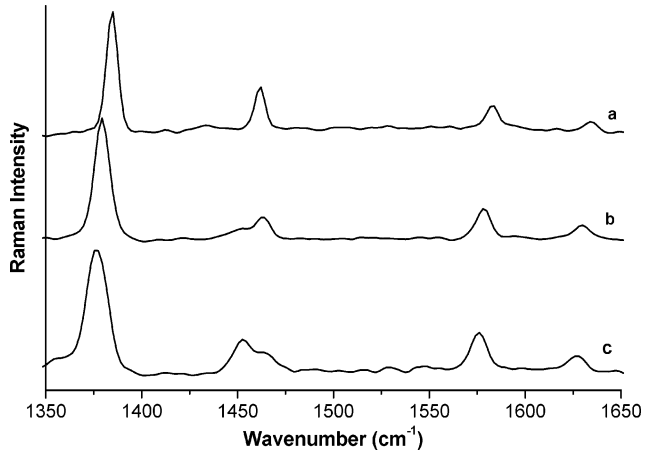

Figure 3. Room-temperature FT-Raman spectra recorded with 1064 nm laser exciting line. (a) 1 NAP@silicalite-1, (b) 1 NAP@$Na_{3.4}$ZSM-5, (c) 1 NAP@$Na_{6.6}$ZSM-5.

(26) Moissette, A.; Marquis S.; Gener I.; Brémard C. *Phys. Chem. Chem Phys.* **2002**, *4*, 5690−5696.

(27) Ohno, K. *J. Mol. Struct*. **1979**, *77*, 329−348.

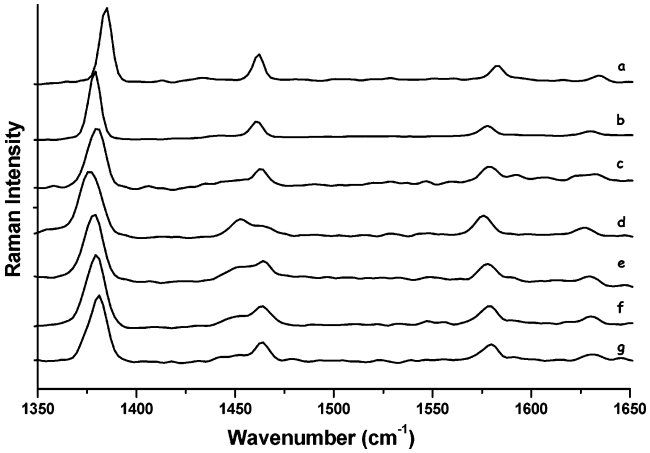

Figure 4. Room-temperature FT-Raman spectra recorded with 1064 nm laser exciting line. (a) 1 NAP@silicalite-1, (b) NAP in chloroform solution, (c) 1 NAP@$Li_{6.6}$ZSM-5, (d) 1 NAP@$Na_{6.6}$ZSM-5, (e) 1 NAP@$K_{6.6}$ZSM-5, (f) 1 NAP@$Rb_{6.6}$ZSM-5, (g) 1 NAP@$Cs_{6.6}$ZSM-5.

solution ones. The most prominent bands were observed at 1583 (m), 1461 (m), 1433 (vw) and 1385 cm^{-1} (s) with relative intensities analogous to that observed in solution. The wavenumber shifts were mainly attributed to the confinement effect because the electrostatic effect in silicalite-1 is assumed to be weak (Figure 2).[12] The entrapment of NAP in the pores of aluminated $Na_{6.6}$ZSM-5 induced marked wavenumber shifts and relative intensity changes. The most prominent Raman bands were observed at 1576 (m), 1464 (w), 1453 (m) and 1376 cm^{-1} (s) (Figure 3). The presence of Al in framework and extraframework Na^+ is related to high electrostatic field in the pores and generates marked changes in the Raman spectra. Moreover, the exchange of Na^+ with Li^+, K^+, Rb^+, Cs^+ leads to marked Raman shifts and relative intensity changes particularly in the 1500−1450 cm^{-1} region (Figure 4). The combined effect of confinement and electrostatic field upon NAP occluded in the pores of M_nZSM-5 induced weak but specific changes according to the nature of extraframework cation M^+. However, the interaction between M^+ and NAP in the channel lowering the local symmetry did not appear to induce break down of the Raman selection rules corresponding to D_{2h} molecular symmetry of NAP molecule. DRUVv, and FT-Raman spectra recorded during the course of the NAP sorption indicate that complete sorption takes place according to eq 9 over more than four weeks in our experimental conditions.

$$\text{NAP} + \text{M}_n\text{ZSM-5} \rightarrow \text{NAP@M}_n\text{ZSM-5} \qquad (9)$$

The resulting DRUVv, and FT-Raman spectra recorded after complete sorption indicate that NAP was sorbed as intact molecule in non Brønsted acidic M_nZSM-5 for $n = 0.0$, 3.0, 3.4, 6.6 and M = Li^+, Na^+, K^+, Rb^+, Cs^+. The close proximity between M^+ and occluded NAP can be assumed from the spectroscopic results.[28]

2. Molecular Modeling of NAP Occluded in M_nZSM-5 Zeolites. The framework structure of bare M_nZSM-5 zeolites and silicalite-1 contains two types of intersecting channels.[29−31] Both are formed by rings of 10 oxygen atoms, characterizing them as a medium-pore zeolite. One channel type is straight and has a nearly circular opening (0.53 × 0.56 nm), while the other one is sinusoidal and has an elliptical opening (0.51 × 0.55 nm). So far, the exact M^+ position has been fully elucidated in bare Cs_nZSM-5 ($n = 3.8$, 5.8) zeolites by X-ray diffraction.[15,32]

The predictions of the energy and structure of NAP sorption site in silicalite-1 host were carried out at 300 K and at constant loading (1 NAP/UC) by Monte Carlo (MC) simulations using the conventional Metropolis algorithm. The calculations took into account the nonbonded interactions between the fixed structure of silicalite-1 and rigid NAP. The details of the MC and subsequent energy minimization calculations have been given in the Experimental Section. The energy distribution of individual NAP exhibits one maximum at −120 kJ mol^{-1} in silicalite-1. The corresponding distributions of the positions occupied by the NAP center of mass indicate that the net potential surface accessible to the molecule is maximum in the straight channel in the vicinity of its intersection with the zigzag channel. The energy minimization procedure leads to NAP occluded in the straight channel at the intersection of the straight and sinusoidal channels along the *b* axis. This sorption site is in accurate agreement with single-crystal diffraction data previously reported for $H_{0.04}$ZSM-5 loaded with 3.68 NAP/UC.[32,33] The siting of the Al atoms in zeolite T sites will be critical information. For M_nZSM-5 with aluminum content, currently no direct experimental information of the Al atom location is available. As used recently for modeling purpose, we distinguish explicitly silicon (T_1−T_{11}) from aluminum sites (T_{12}) with partial and random occupation according to the aluminum content *n*.[16] Because of the strong Coulombic interactions with the zeolite framework, the energetically most favorable positions for the M^+ cations are near the O atoms binding Al atoms. The nearest distances between M^+ and O atoms obtained after an energy minimization procedure with the zeolite framework fixed and the M^+ mobile were found to be in reasonable agreement with theoretical and experimental studies previously reported.[15,34] The resulting zeolite structures were used to predict the energy and structure of NAP sorption site in M_nZSM-5 by MC simulations at 300 K with 1 NAP/UC loading (see Experimental Section). The energy distribution of individual NAP exhibits one maximum at −125 kJ mol^{-1} in Li_4ZSM-5. The corresponding distributions of the positions occupied by the NAP center of mass indicate that the net potential surface accessible to the molecule is maximum in the straight channel in the vicinity of Li^+ cation with NAP lying in the straight channel along the *b* direction with phenyl groups facially coordinated to the Li^+ cation. The sorption of NAP is expected to influence the location of M^+ in the framework. Thus, the energy minimization procedure taking NAP and Li^+ as mobile leads to an analogous structural situation as obtained by MC (Figure 5).

Similar results were obtained for M = Na^+, K^+, Rb^+, Cs^+. The simulated structural situation of NAP@Cs_4ZSM-5 was found to be in reasonable agreement with XRD data related to xylene occluded in $Cs_{3.8}$ZSM-5.[32] The repartition of the energy

(28) Thomas, K. J.; Sunoj, R. B.; Chandrasekhar, J.; Ramamurthy, V. *Langmuir* **2000**, *16*, 4912−4921.
(29) Van Koningsveld, H.; Jansen, J. C.; Van Bekkum, H. *Zeolites* **1990**, *10*, 235−242.
(30) Van Koningsveld, H. *Acta Crystallogr.* **1990**, *B46*, 731−735.
(31) Van Koningsveld, H.; Jansen, J. C.; Van Bekkum, H. *Zeolites* **1987**, *7*, 564−568.
(32) Mentzen, B. F.; Gélin, P. *Mater. Res. Bull.* 1998, *33*, 109−116.
(33) Van Koningsveld, H.; Janssen, J. C. *Microporous Mater.* **1996**, *6*, 159−167.
(34) Kucera, J.; Nachtigall, P. *Phys. Chem. Chem. Phys.* **2003**, *5*, 3311−3317.

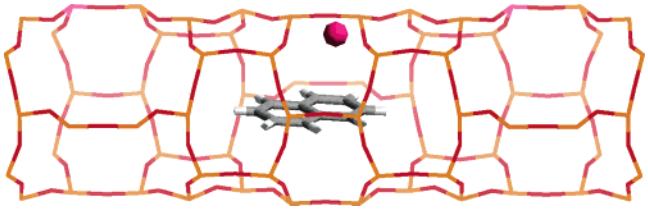

Figure 5. Predicted sorption site of NAP in the straight channel of Na_4ZSM-5 (1 NAP/UC). Red, yellow, and pink lines represent the O, Si, and Al atoms of the $[(AlO_2)_4(SiO_2)_{92}]^{4-}$ framework, respectively. The white and shaded cylinders represent the H and C atoms of the NAP ($C_{10}H_8$) molecule, respectively. The red sphere represents the Na^+ cation.

in van der Waals energy and electrostatic energy indicates the major role of the electrostatic interactions, particularly through the M^+-phenyl group interactions with respect to the corresponding repartition of the energy.[35] The openings of the straight channels of M_nZSM-5 are sufficiently wide to allow NAP molecules to pass through them and to diffuse slowly into the void space to the sorption site with the phenyl group facially coordinated to the M^+ cation in close proximity to the Al atom.

3. Diffuse Reflectance UV−Visible Absorption of Persistent Charge Carriers Generated by Photoionization of NAP@M_nZSM-5. A laser operating at a 266-nm wavelength was used during 15 s to irradiate the samples (see Experimental Section). The photolysis wavelength falls within the contour of the electronic transitions of NAP occluded in M_nZSM-5 (Figure 1). The DRUVv spectra carried out after UV irradiation of NAP and occluded in purely siliceous silicalite-1 ($n = 0$) did not provide any evidence of durable new species at room temperature. In contrast, after the 15-s irradiation period of aluminum-rich NAP@M_nZSM-5, many DRUVv spectra were recorded during several hours and provided evidence of durable new species. The DRUVv spectra recorded after the photolysis are shown in Figure 6A.

The data processing of each huge spectral set recorded between 340 and 800 nm for all the irradiated NAP@M_nZSM-5 samples ($n = 3.4$, 6.6; M = Li^+, Na^+, K^+, Rb^+, Cs^+) was carried out using the SIMPLISMA approach (see Experimental Section) and was found to resolve the characteristic spectra of pure species from the mixture generated by photolysis. Two pure spectra were extracted from each spectral set with accurate agreement between calculated and experimental spectra. The two resolved DRUVv spectra were shown in Figure 6 B. The first spectrum to be extracted displays characteristic narrow bands at 367, 382, 567, 597, 616, 653, 674 nm (Figure 6B, spectrum a). This typical spectrum was found to be detected for all the samples and was readily assigned to the occluded radical cation $NAP^{\bullet+}$ by comparison with previous UV−visible investigations of $NAP^{\bullet+}$ trapped in solid Ar at low temperature.[36−38] The second spectrum to be resolved exhibits broad absorption bands centered at ca. 500 nm with at least two maxima more or less resolved. The two bands obtained after spectral decomposition of these absorption features are listed in Table 1. The wavelengths of the bands hardly change according to the nature of M^+ of irradiated NAP@M_nZSM-5

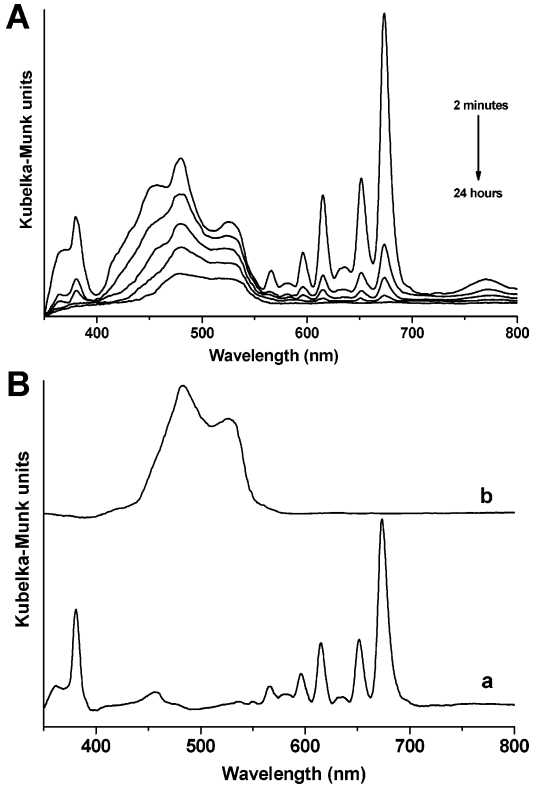

Figure 6. (A) Diffuse reflectance UV−vis (DRUVv) absorption spectra recorded from 2 min to 24 h after the irradiation was stopped for 1 NAP@$Li_{6.6}ZSM-5$ (photolysis 266 nm, 15 s, 30 mJ cm^{-2}). (B) UV−vis absorption spectra resolved by the SIMPLISMA approach (a) $NAP^{\bullet+}$@ $Li_{6.6}ZSM-5^{\bullet-}$, (b) NAP@ $Li_{6.6}ZSM-5^{\bullet-\bullet+}$.

samples, while the energy difference between the two maxima was found to be constant and to correspond to ~1600 cm^{-1}. The prominent absorption bands were correlated with the creation of the electron−hole pair.[39] Data processing of spectral sets using SIMPLISMA software resolved also the respective contribution C of each absorbing species as a function of time. Normalization of $C(t) = C/C_0 = 1$ at $t = 0$ (excitation off) was used to obtain the relative contribution of each species. Panels A and B of Figure 7 exhibit the specific $C(t)$ decays of $NAP^{\bullet+}$ (curves a) and charge-transfer species (curves b) measured after the photolysis of NAP@$Li_{6.6}ZSM-5$ (A) and NAP@$Li_{3.4}ZSM-5$ (B), respectively. Figure 7, A, B, is typical of all the attempts made after the photolysis of NAP@M_nZSM-5 ($M^+ = Li^+$, Na^+, K^+, Rb^+, Cs^+ and $n = 3.4$, 6.6).

$$\text{NAP@M}_n\text{ZSM-5} + h\nu \rightarrow \text{NAP}^{\bullet+}\text{@M}_n\text{ZSM-5}^{\bullet-} \quad (10)$$

For all irradiated NAP@M_nZSM-5 samples, the formation of the $NAP^{\bullet+}$−electron pairs was found to be very fast according to eq 10 and occurs probably according to photonic processes previously described in solution.[7] The $NAP^{\bullet+}$ (curve a) contribution was found to decrease to zero over less than 1 h, whereas the concentration of the electron−hole was found to decrease more slightly to reach a plateau corresponding to a stable charge-separated state. The rate of the electron−hole pair formation was not determined but is expected to be correlated to $NAP^{\bullet+}$ disappearance. The bands centered on 500 nm were found to

(35) Nicholas, J. B.; Hay, B. P.; Dixon, D. A. *J. Phys. Chem. A* **1999**, *103*, 1394−1400.
(36) Andrews, L.; Kelsall, B. J.; Blankenship, T. A. *J. Phys. Chem.* **1982**, *86*, 2916−2926.
(37) Kelsall, B. J.; Andrews, L. J. *Chem. Phys.* **1982**, *76*, 5005−5013.
(38) Andrews, L.; Blankenship, T. A. *J. Am. Chem. Soc.* **1981**, *103*, 5977−5979.
(39) Gener, I.; Moissette, A.; Brémard, C. *Phys. Chem. Chem. Phys.* **2004**, *6*, 3732−3738.

Table 1. Kinetic and Spectroscopic Results of $NAP^{\bullet+}$−electron and Electron−Hole Pairs after Photolysis of 1 NAP@M_nZSM-5 (266 nm, 15 s, 30 mJ/cm^2)

$M_{6.6}$ZSM-5 M	$NAP^{\bullet+}$–electron[a] $\bar{k}_1$ mn^{-1} (γ)	electron–hole bands[b] max(nm)	electron–hole[a] $\bar{k}_{2s}$ mn^{-1} (γ)	electron–hole[c] yield %	electron–hole[c] distance (nm)
Li^+	2.7×10^{-1} (1.7)	482; 525	$\ll 10^{-3}$	90	1.39 ± 0.05
Na^+	3.8×10^{-2} (2.0)	481; 525	2.3×10^{-3} (1.1)	30	1.25 ± 0.05
K^+	2.7×10^{-1} (1.3)	482; 520	1.8×10^{-2} (1.4)	50	1.28 ± 0.05
Rb^+	2.6×10^{-1} (1.5)	480; 530	1.7×10^{-2} (1.9)	30	1.37 ± 0.05
Cs^+	1 (1)	482; 528	$2{,}8 \times 10^{-2}$ (2.1)	50	1.25 ± 0.05
$M_{3.4}$ZSM-5 M	$NAP^{\bullet+}$–electron[a] $\bar{k}_1$ mn^{-1} (γ)	electron–hole bands[b] max(nm)	electron–hole[a] $\bar{k}_{2s}$ mn^{-1} (γ)	electron–hole[c] yield %	electron–hole[c] distance (nm)
Li^+	5×10^{-2} (1.3)	482; 525	$<10^{-3}$	50	1.32 ± 0.05
Na^+	1.5×10^{-1} (1.2)			5	
K^+	3.3 (1.4)			∼0	
Rb^+	2.4×10^{-1} (2.9)			∼0	
Cs^+					

[a] $\bar{k}$ is the average first-order rate constant with corresponding (γ) distribution coefficient deduced using the Albery function of the concentration values resolved by SIMPLISMA processing of DRUVv spectra. [b] UV−visible characteristic absorption band obtained by spectral decomposition of the charge-transfer band resolved by the SIMPLISMA processing. [c] Obtained from EPR measurements (see text).

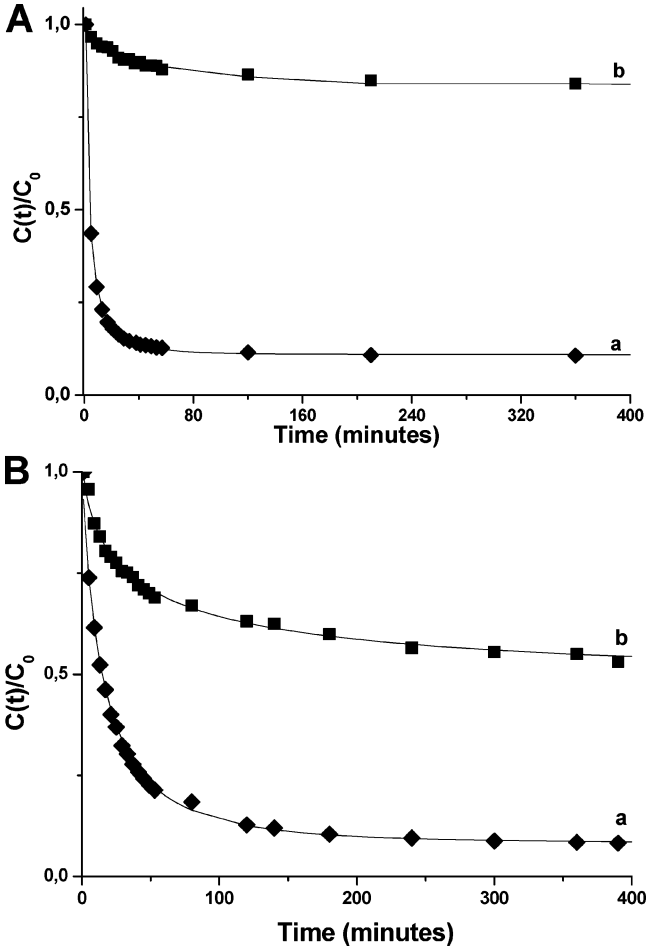

Figure 7. (A) Decay profiles of $C(t)/C_0$ relative to concentrations of: (a) $NAP^{\bullet+}$@$Li_{6.6}$ZSM-$5^{\bullet-}$, (b) NAP@$Li_{6.6}$ZSM-$5^{\bullet-\bullet+}$. (B) Decay profiles of $C(t)/C_0$ relative to concentrations of: (a) $NAP^{\bullet+}$@$Li_{3.4}$ZSM-$5^{\bullet-}$, (b) NAP@$Li_{3.4}$ZSM-$5^{\bullet-\bullet+}$. The $C(t)/C_0$ values were extracted using the SIMPLISMA approach of the DRUVv spectra recorded after the photolysis of 1 NAP@Li_nZSM-5 (266 nm, 15 s, 30 mJ cm^{-2}). The solid lines represent the best calculated decays using the Albery function (see Experimental Section).

be persistent over more than several hours after complete disappearance of the $NAP^{\bullet+}$ bands. Analysis of the decay curves using a first-order model of discrete exponentials was not found to be satisfactory. The complexity of the $NAP^{\bullet+}$ decays was found to be due to heterogeneity of the microenvironments of $NAP^{\bullet+}$ and a distribution of rate constants should be considered instead. In principle, the exponential series method, the maximum entropy method, and the stretched exponentials could solve the problem. However, the $NAP^{\bullet+}$ decays were accurately simulated according to the Albery kinetic model detailed in the Experimental Section. The best values of the first-order $\bar{k}_1$ average rate constants with the corresponding γ Gaussian distribution coefficients deduced by the fitting procedure are listed in Table 1. In view of the randomness of the residuals, curve fittings with the Albery kinetic model were found to be satisfactory. $NAP^{\bullet+}$ was assumed to disappear according to two parallel competitive ways: direct charge recombination ($\bar{k}_{1r}$) and electron transfer ($\bar{k}_{1t}$) with $\bar{k}_1 = \bar{k}_{1r} + \bar{k}_{1t}$.

$$\mathbf{NAP^{\bullet+}@M_nZSM\text{-}5^{\bullet-}}\ (\bar{k}_{1r}) \rightarrow \mathbf{NAP@M_nZSM\text{-}5} \quad (11)$$

$$\mathbf{NAP^{\bullet+}@M_nZSM\text{-}5^{\bullet-}}\ (\bar{k}_{1t}) \rightarrow \mathbf{NAP@M_nZSM\text{-}5^{\bullet-\bullet+}} \quad (12)$$

The electron-transfer rate ($\bar{k}_{1t}$) was assumed to be relatively faster than the direct charge recombination ($\bar{k}_{1r}$). The disappearance of $NAP^{\bullet+}$ was found to be indicative of high-yield electron transfer (eq 12) only for $NAP^{\bullet+}$@$Li_{6.6}$ZSM-$5^{\bullet-}$ ($\bar{k}_{1t} \gg \bar{k}_{1r}$, Figure 7A). In contrast, the proportion of charge recombination was estimated to be approximately 50% for $NAP^{\bullet+}$@$Li_{3.4}$ZSM-$5^{\bullet-}$ ($\bar{k}_{1t} > \bar{k}_{1r}$, Figure 7B). The facile abstraction of one electron from the zeolite framework took place because of the oxidizing power of $NAP^{\bullet+}$ ($E_{ox} = 1.5$ V vs SCE). Analogous behavior was reported recently for biphenyl radical cation ($E_{ox} = 1.9$ V vs SCE) but did not occur for radical cation anthracene ($E_{ox} = 1.1$ V vs SCE).[40,41] It is clear that the rates of both electron transfer and $NAP^{\bullet+}$−electron recombination highly depend on both the aluminum content (n) and on the nature of extraframework cation M^+ (Table 1). The cationic exchange from Li^+ to Cs^+ is expected to increase the basicity of framework oxygen and particularly the basicity of O atoms linked to Al(III), which is expected to enhance the electron-donor properties of the zeolite framework.[4] The specific rate of the electron−hole pair recombination (eq 13) was measured

(40) Morkin, T. L.; Turro, N. J.; Kleinman, M. H.; Brindle, C. S.; Kramer, W. H.; Gould, I. R. *J. Am. Chem. Soc.* **2003**, *125*, 14917−14924.
(41) Vezin, H.; Moissette, A.; Brémard, C. *Angew. Chem., Int. Ed.* **2003**, *42*, 5587−5591.

through the decay of the charge-transfer spectrum (Figure 7 A,B, curves b).

$$\mathbf{NAP@M_nZSM\text{-}5}^{\bullet-/\bullet+}\ (\bar{k}_{2s}, \bar{k}_{2r}) \rightarrow \mathbf{NAP@M_nZSM\text{-}5} \quad (13)$$

The decay occurs according to both slow recombination ($\bar{k}_{2s}$) and very long-time recombination regimes ($\bar{k}_{2r}$). The rate constant ($\bar{k}_{2r}$) of the very long-time regime was assumed to be zero on the time scale of the experiments. The slow recombination decays were accurately simulated according to the Albery kinetic model. The best values of $\bar{k}_{2s}$ average rate constants with the corresponding γ distribution coefficients deduced from the fitting procedure are listed in Table 1. The yields of the very long-lived charge-separated state were measured at $t = 12$ h with respect to the charge separation yield measured 2 min after irradiation ceased. The yield values are listed in Table 1. It is clear that rate of slow electron−hole recombination and the yield of very long-lived electron−hole pairs highly depend both on the aluminum content (n) and the nature of extraframework cation M (Table 1). The electron−hole pair NAP@$Li_{6.6}$ZSM-$5^{\bullet-\bullet+}$ was found particularly stable at room temperature over more than several weeks. The yield of the NAP@$M_{3.3}$ZSM-$5^{\bullet-\bullet+}$ electron−hole pair was found to be weak except for NAP@$Li_{3.3}$ZSM-$5^{\bullet-\bullet+}$. The electron−hole recombination rate appears in relation to both the nature of the extraframework cation and aluminum distribution in the framework.

4. Electron Paramagnetic Resonance of Persistent Charge Carriers Generated by Photoionization of NAP@M_nZSM-5. The use of CW-EPR measurements to study paramagnetic species generated by laser irradiation played a major role for understanding NAP photoionization.[11] As reported previously, the EPR spectra of bare M_nZSM-5 zeolites did not exhibit any detectable paramagnetic species.[39,42] No EPR signal was detected after NAP was embedded in nonacidic M_nZSM-5, indicating that no detectable ionization dark reaction occurs. In contrast, intense EPR signals were previously reported after mere exposure of NAP to calcined acidic H_nZSM-5 under argon and at room temperature.[13] The CW-EPR spectra carried out after UV irradiation of NAP occluded in silicalite-1 ($n = 0$) did not generate durable paramagnetic species at room temperature. However, when the photolysis was carried out at 77 K, the resulting EPR spectra were found to be due to occluded $NAP^{\bullet+}$ as observed previously in aluminum-poor ZSM-5 at low temperature.[11] In contrast, durable EPR signals were detected at room temperature after photolysis of NAP occluded in aluminum-rich M_nZSM-5 zeolites ($n = 3.4$, 6.6; M=Li^+, Na^+, K^+, Rb^+, Cs^+) according to eq 10. The fate of the photogenerated species with time was monitored by EPR measurements at room temperature. Numerous EPR spectra were recorded at different times after the photolysis (Figure 8). The EPR spectra recorded immediately after the irradiation off exhibit the characteristic features of the $NAP^{\bullet+}$ spectrum superimposed on a broad signal. The well-resolved peaks evolved over less than 1 h to broad signals.

The double integrated values of overall signals were shown as a function of time in Figure 9, A and B, for irradiated NAP@$Li_{6.6}$ZSM-5 and NAP@$Li_{3.4}$ZSM-5 samples, respectively. It appears clearly that concentration of the paramagnetic species decreases during the first hour following photolysis before reaching a plateau. The persistence and the remaining quantity of the paramagnetic species were found to increase according

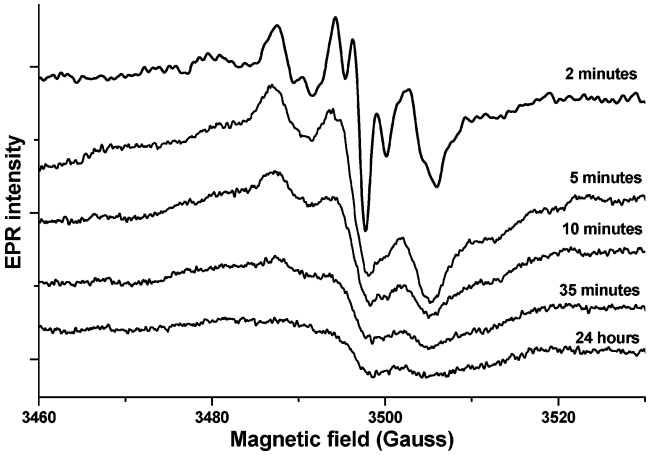

Figure 8. Room-temperature X-band CW-EPR spectra recorded from 2 min to 24 h after the irradiation was stopped for 1 NAP@$Na_{6.6}$ZSM-5 (photolysis: 266 nm, 15 s, 30 mJ cm^{-2}).

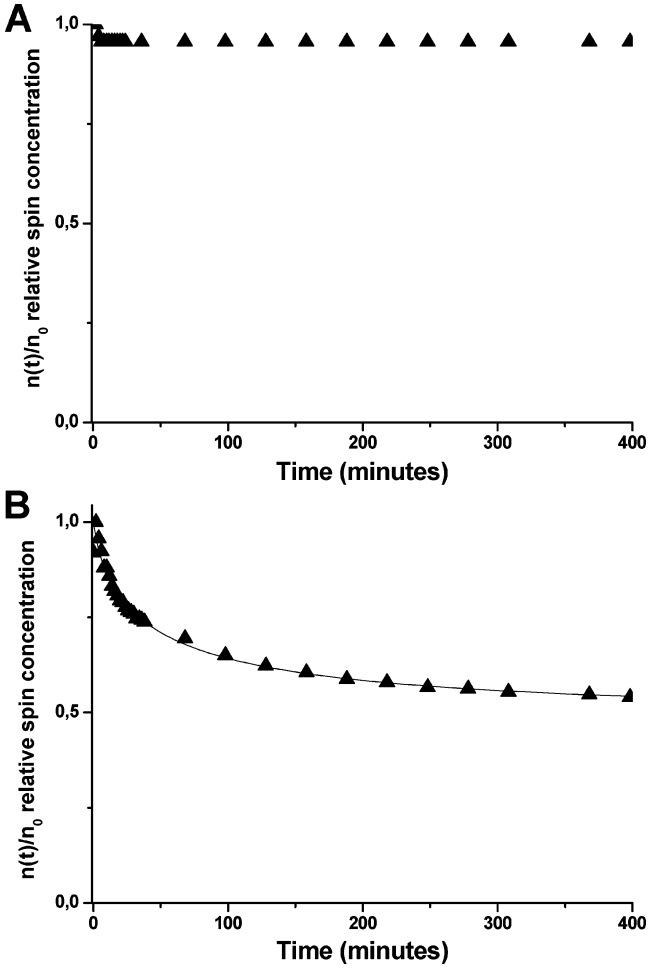

Figure 9. (A) Decay profile of $n(t)/n_0$ relative spin concentration of both $NAP^{\bullet+}$@$Li_{6.6}$ZSM-$5^{\bullet-}$ pair and NAP@$Li_{6.6}$ZSM-$5^{\bullet-\bullet+}$ electron−hole pair. (B) Decay profile of $n(t)/n_0$ relative spin concentrations of both $NAP^{\bullet+}$@$Li_{3.4}$ZSM-$5^{\bullet-}$ pair and NAP@$Li_{3.4}$ZSM-$5^{\bullet-\bullet+}$ electron−hole pair. The $n(t)/n_0$ values were calculated by double integration of the EPR spectra recorded after the irradiation off (photolysis of 1 NAP@Li_nZSM-5: 266 nm, 15 s, 30 mJ cm^{-2}). The solid lines represent the best calculated decays using the Albery function (see Experimental Section).

(42) Staudte, B.; Gutsze, A.; Böhlmann, W.; Pfeifer, H.; Pietrewicz, B. *Microporous Mesoporous Mater.* **2000**, *40*, 1−7.

to the following order $Cs^+ < Rb^+ < K^+ < Na^+ < Li^+$ and were found also to increase with the aluminum content of the zeolite (Table 1). The remaining spin quantity was found to be particularly low for NAP@$Cs_{3,4}$ZSM-5 irradiated sample and particularly high for NAP@$Li_{6.6}$ZSM-5 (Figure 9B). The residual EPR signals were found to be stable over several weeks at room temperature. The electron−hole recombination appears to proceed according to both long-time and very long-time regimes (eq 13). The Albery heterogeneous kinetic model was found to fit reasonably the decay curves of the spin quantity corresponding to the slow electron−hole recombination with $\bar{k}_{2s}$ constant value in reasonable agreement with the values obtained by DRUVv measurements (Table 1). However, no satisfactory explanation at the atomic scale can be obtained with this model. The recombination kinetics of trapped carriers by tunneling processes was considered and Shklovskii and coworkers proposed a detailed model that describes recombination kinetics of photogenerated carriers.[24] The explicit development of the model used in this report was shown before and is briefly summarized in the Experimental Section.[25] The basic assumption of the model is that spatially close electron−hole pairs have a much higher recombination rate than distant pairs with the condition that the number of electrons is equal to the number of holes. It follows that, after some time t, spatially close electron−hole pairs will have recombined, thus leaving carriers with larger distances behind. The nearest-neighbor distance increases and can be written as $\boldsymbol{r}(t) = \boldsymbol{a}/2 \cdot \ln(\nu_0 \cdot t)$ (eq 6), where ν_0 may be interpreted as an attempt to recombine frequency and $\boldsymbol{a}$ describes an effective localization radius assumed to be the same for the electron and the hole. At very long times, i.e., at large $\boldsymbol{r}$ the remaining electron−hole pairs $\boldsymbol{n}$ represented by the spin quantity (Figure 9AB) are written as

$$\boldsymbol{n}(r) = [(4\pi/3)\,\boldsymbol{r}^3]^{-1} = [\pi/6\,\boldsymbol{a}^3 \ln^3(\nu_0.t)]^{-1} \qquad (14)$$

from which follows that the very long-time residual electron−hole pair concentration is independent of the initial electron−hole density and also $NAP^{\bullet+}$−electron yield. This picture is in accordance with electrons and holes localized in deep traps of the zeolite framework. The long-lived charge separation proceeds via a sequence of electron transfers described above. To obtain magnetic and structural information from these very long-lived electron−hole pairs (Table 1) we perform simulations of the CW-EPR spectra obtained a long time after the photolysis off. The experimental spectra were recorded at room temperature several days after the photolysis. EPR spectrum of two $S = {}^1/_2$ spins coupled by isotropic and anisotropic interactions has been extensively discussed in textbooks and in reviews and particularly the cases of weakly interacting spins.[43,44] We consider the pair of radicals A and B ($S_{A,B} = {}^1/_2$) separated by a distance large enough to make exchange and dipole spin−spin interactions small compared to the difference between the resonance frequencies of individual radicals, that is $\omega_{SS} \ll |\omega_A - \omega_B|$. Under these conditions, the Hamiltonian can be truncated to the secular part.[45]

$$H = \omega_A S_{Az} + \omega_B S_{Bz} + \omega_{SS} S_{Az} S_{Bz} \qquad (15)$$

where ω_A and ω_B contain the electronic Zeeman term $\mu_B B \cdot g \cdot S$, and others terms (hyperfine, quadripolar, nuclear Zeeman), ω_{SS} is the sum of the exchange and dipole−dipole interaction terms,

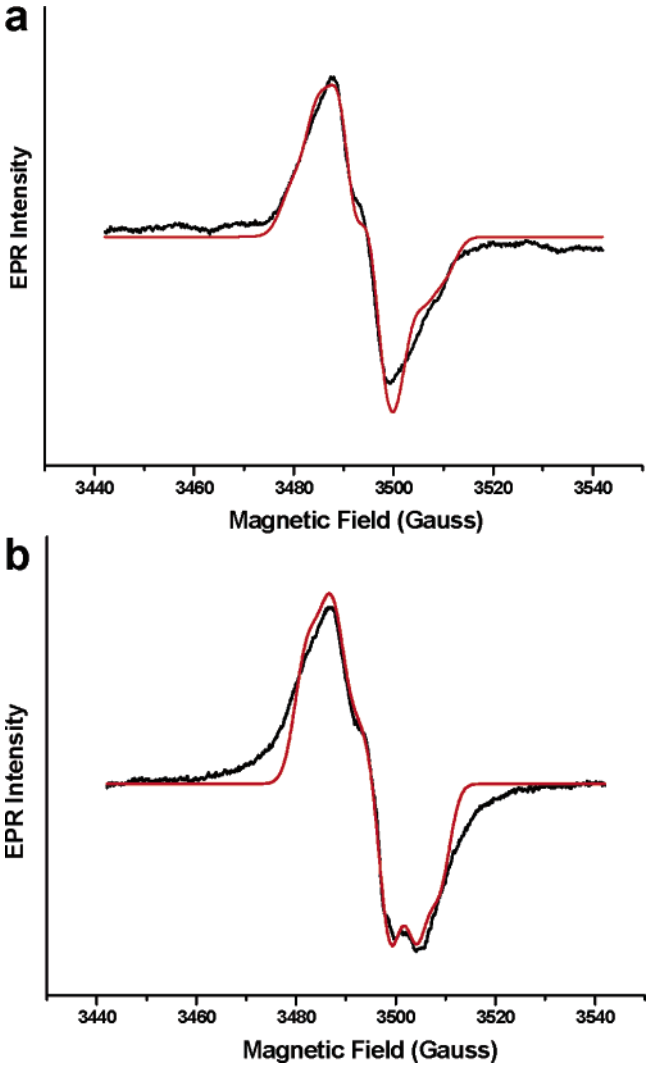

Figure 10. (a) Room-temperature experimental and simulated X-band CW-EPR spectra recorded 48 h after the UV irradiation of 1 NAP@$Li_{6.6}$ZSM-5 (photolysis: 266 nm, 15 s, 30 mJ cm^{-2}). (b) Room-temperature experimental and simulated X-band CW-EPR spectra recorded 48 h after the UV irradiation of 1 NAP@$Li_{3,4}$ZSM-5 (photolysis: 266 nm, 15 s, 30 mJ cm^{-2}). The experimental spectra are shown by black lines, and the simulated spectra with the parameters of Table 1 and the Experimental Section are shown by red lines.

that is, $\omega_{SS} = (J + D)$. The exchange parameter J is defined as the energy splitting between the singlet and triplet spin state. The dipole splitting term, D, has the well-known dependence on the distance between the paired radicals, r_{AB}, and on the angle θ_{AB} between the pair director and external field. The other terms have their usual meanings.

$$D = (\beta^2 g_A g_B/\hbar r^3_{AB})(1 - 3\cos^2\theta_{AB}) \qquad (16)$$

The CW-EPR spectra of the long-lived electron−hole pairs in high yield (Table 1) were simulated numerically, taking into account the random orientation of powders of the samples (Figure 10a,b).

(43) Bencini, A.; Gatteschi, D. *Electron Paramagnetic Resonance of Exchange Coupled Systems*; Springer: Berlin, 1990; Chapter 3.
(44) Eaton, G. R.; Eaton, S. S. In *Biological Magnetic Resonance*; Berliner, L. J., Reuben, J., Eds.; Plenum: New York, 1989; Vol. 8, pp 339−396.
(45) Dubinski, A. A.; Perekhodtsev, G. D.; Poluektov, O. G.; Rajh, T.; Thurnauer, M. C. J. *Phys. Chem. B* **2002**, *106*, 938−944.

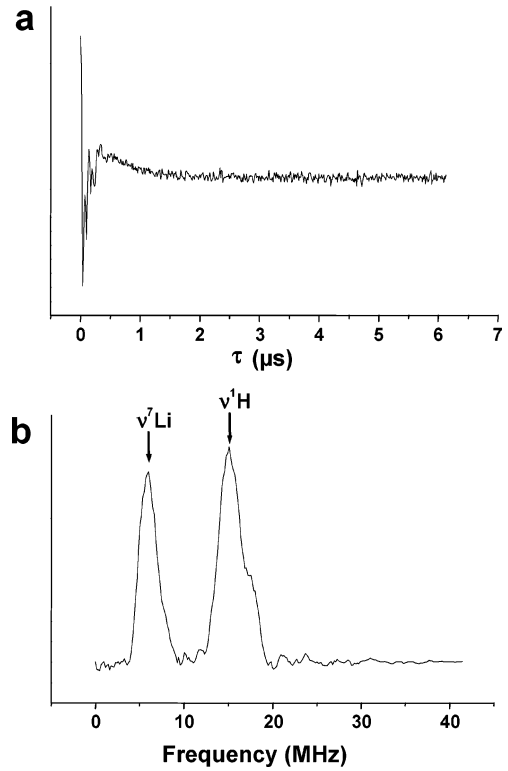

Figure 11. (a) Two-pulse ESEEM time domain of NAP@$Li_{6.6}$ZSM-5$^{\bullet-\bullet+}$ electron−hole pair recorded at 4 K and (b) Fourier transform of ESEEM spectrum of the time domain. A Hamming function apodization was used prior FFT.

The best values of J and D, were obtained after a fitting procedure of $d\chi''/dB$ with an angular independent (isotropic) line width of EPR lines where the g, Euler angle values, D and J were allowed to vary. Reasonable agreement was obtained between experimental and calculated $d\chi''/dB$ values with $J \approx 0$ and D around 40 MHz. The distances between the electron and hole listed in Table 1 were deduced from the D values obtained by the fitting procedure. All the distances were found to be around 1.3 nm within the error range (Table 1). The electron-transfer rate for charge recombination of a very long-lived electron−hole pair can be described by the Marcus theory.[46] The maximum rate of the electron transfer can be related to the exchange interaction, J.[47,48] The very low rate constant was found to be in reasonable agreement with the very low value ($J \approx 0$) of the magnetic exchange.

The spectral resolution of CW-EPR is not sufficient to resolve the hyperfine interaction of the unpaired electron with the alkali metal ion. The electron spin−echo envelope modulation (ESEEM) is a very useful method to investigate superhyperfine interactions; as such, it has been applied to study the close surroundings of paramagnetic centers in a variety of systems. Many new ESEEM experiments have been designed during the past 15 years which offer various possibilities for structural studies of disordered systems.[49] We used both the one-dimensional (1D) two-pulse ESEEM experiment and the (2D) version of the four-pulse ESEEM sequence. In particular, the

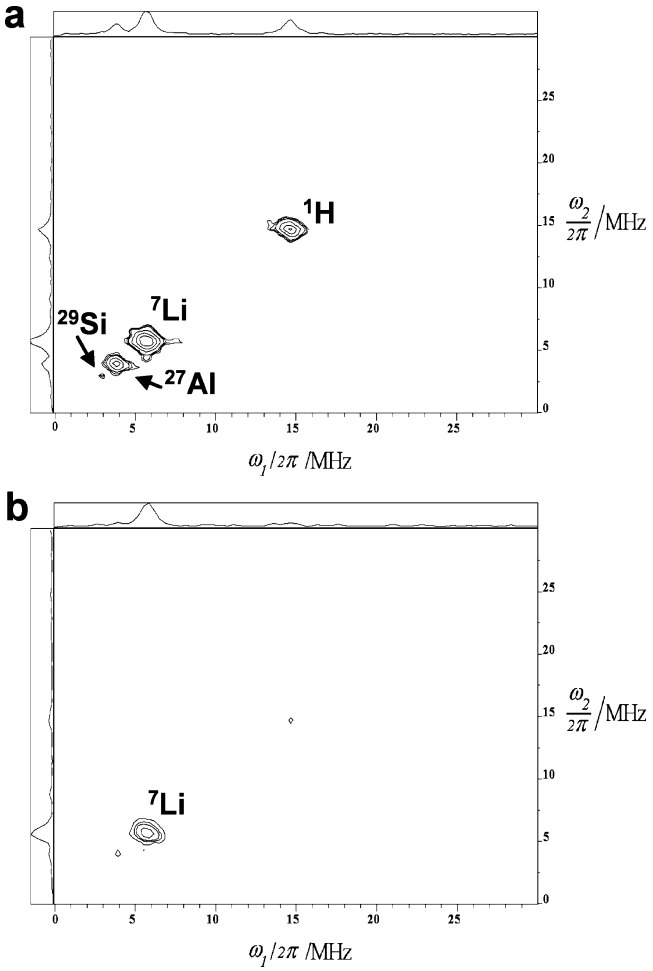

Figure 12. 2D-HYSCORE spectra of NAP@$Li_{6.6}$ZSM-5$^{\bullet-\bullet+}$ electron−hole pair recorded at 4.2 K. $\pi/2$ and π pulses were respectively 12 ns and 24 ns; 256 × 256 data set was apodized using Hamming function prior to Fourier transform and magnitude calculation. (a) τ = 88 ns; (b) τ = 156 ns.

2D approach of hyperfine sublevel correlation (HYSCORE) has especially been proven to be a powerful tool for the determination of weak hyperfine and nuclear quadrupole interactions included in the ω_A and ω_B terms of Hamiltonian (eq 15). The exchange and dipolar interactions between the two unpaired electrons of the electron−hole pair were reported previously to have no significant effect on the ESEEM spectra if their strength is small compared to the difference in EPR frequencies of the two electrons.[50,51] Two days after laser photolysis, the NAP@$Li_{6.6}$ZSM-5$^{\bullet-\bullet+}$ sample was cooled to 4 K. The CW spectra recorded consisted of a broad band of 25 G. The two pulses ESEEM time domain spectrum (Figure 11 a) showed a fast relaxation of the signal; consequently, only the initial modulation signal was recorded. This phenomenon is due to a short phase memory time T_m of 140 ns. The Fourier transform of the time domain signal only showed the nuclear Larmor frequency of the ^{7}Li isotope (5.9 MHz) and the proton frequency at 14.5 MHz (Figure 11 b). The results of the 2D-HYSCORE experiments for two τ values of 88 and 156 ns are displayed in Figure 12 a,b. For the both τ values only diagonal nuclear Larmor frequency was observed. For a τ value of 88 ns ^{1}H,

(46) Marcus, R. A.; Sutin, N. *Biophys. Acta* **1985**, *82*, 534−322.
(47) Girerd, J. J.; Journaux, Y.; Kahn, O. *Chem. Phys. Lett.* **1981**, *82*, 534−538.
(48) Calvo, R.; Abresch, E. C.; Bittl, R.; Feher, G.; Hofbauer, W.; Isaacson, R. A.; Lubitz, W.; Okamura, M. Y.; Paddock, M. L. *J. Am. Chem. Soc.* **2000**, *122*, 7377−7341.
(49) Matar, K.; Goldfarb, D. *J. Chem. Phys.* **1992**, *96*, 6464−6476.
(50) Tan, J.; Thurnauer, M. C.; Norris J. R. *Chem. Phys. Lett.* **1994**, *219*, 283−290.
(51) Zwanenburg, G.; Hore, P. J. *J. Magn. Res.* **1994**, *114*, 139−146.

^{7}Li, ^{27}Al, and ^{29}Si frequencies were observed at respectively 14.5, 5.9, 3.9, and 2.9 MHz. By increasing the τ value only the ^{7}Li signal remained due to a strong T_1 suppression effect. For the 2D HYSCORE spectrum recorded at $\tau = 88$ ns only Larmor nuclear frequencies on the (+,+) quadrant were detected; thus, no antidiagonal cross-peak could be measured. As a result of the isotropic coupling and the dipolar component the **A** tensor is very small and less than the Larmor nuclear frequency. Consequently, it means a very small fraction of the electrons populated the 2s Li orbital, resulting in non-measurable isotropic hyperfine coupling, contrary to those observed for radical cation−electron pairs generated by spontaneous ionization of anthracene in Li$_n$ZSM-5.[52] With the present results it is not possible to discern the respective environment of the trapped electron and the positive hole. The electron can be located in a limited space around one Li^+ close to Si−O−Al bridge and the occluded NAP with low population of the 2s Li orbital vacancy. The positive hole can be assumed to be located on the oxygen atom of another Si−O−Al bridge close to another Li^+ cation. The separation distance of the electron and hole of 1.3 nm can be in the range of Al- - -Al distance.

The previously reported 2D HYSCORE spectrum of the long-lived electron−hole pair NAP@$H_{3.4}$ZSM-5$^{\bullet-\bullet+}$ initiated by NAP sorption in acidic $H_{3.4}$ZSM-5 zeolite indicates a pair of "ridges" centered at the ^{1}H nuclear Larmor frequency corresponding to ^{1}H anisotropic constant of 7 MHz. A weak ^{13}C coupling was observed in the (+, +) f_2 domain with an anisotropic of 3.7 MHz. However, no signal feature from the zeolite nuclei interaction through ^{29}Si or ^{27}Al was observed.[13] In contrast, the HYSCORE spectrum of the electron−hole correlated pair obtained by biphenyl sorption in acidic $H_{3.4}$ZSM-5 shows ^{29}Si and ^{27}Al Larmor diagonal frequencies and displays also five ridges centered at the ^{1}H Larmor frequency, corresponding to a 9 MHz anisotropic hyperfine constant. The spin−echo correlation spectra (SECSY) of these correlated electron−hole pairs trapped in M$_n$ZSM-5 zeolites were found to be consistent with isolated unpaired electron behavior coupled with nuclei of the surrounding.[53]

Discussion

The present results indicate that NAP molecules are sorbed as intact molecules in the pores of non-Brønsted acidic M$_n$ZSM-5 zeolites with $M_n(AlO_2)_n(SiO_2)_{96-n}$ unit cell composition (n = 3.0, 3.4, 6.6; M = Li^+, Na^+, K^+, Rb^+, Cs^+). The Raman scattering and UV−visible absorption spectrometry demonstrate the specific influence of the extraframework cation M^+ upon the facial coordination of NAP. The molecular modeling provides reasonable structural parameters of the preferred NAP sorption sites in M$_n$ZSM-5 zeolites. The NAP molecule lies preferentially in the straight channel with phenyl groups facially coordinated to the extraframework cation. These results were found to be in accurate agreement with previous modeling and X-ray diffraction data of polyaromatic molecules occluded in zeolites and particularly in ZSM-5.[3,17,20,32,33]

The photoionization of NAP occluded in the straight channel of non-Brønsted acidic ZSM-5 zeolites generates primary NAP$^{\bullet+}$−electron pair as fast phenomenon. The photoinduced charge separation was stabilized by a subsequent electron transfer from the zeolite framework to electron-deficient NAP$^{\bullet+}$ to generate long-lived spin-correlated distant electron−hole pairs.[4] The ionization yield was found to be particularly high for aluminum-rich ZSM-5 with Li^+ as a counter-balancing cation, and the lifetime of these electron−hole pairs was found to be stable more than several weeks in the void space of $Li_{6.6}$ZSM-5. This very long charge separation was found to be unusual with respect to the lifetime of the photoinduced charge separated state exhibited in solution and in faujasitic zeolites. The electron−hole pair generated by photolysis of NAP occluded in $Li_{6.6}$ZSM-5 appears more stable than other long-lived photoinduced charge separation in heterogeneous media recently reported.[54] The electron−hole pairs NAP@M$_n$ZSM-5$^{\bullet+\bullet-}$ stabilized in nonacidic M$_n$ZSM-5 zeolites exhibit characteristic broad bands in the 480−530 nm region (Table 1). Analogous bands in the 450−500 nm range were previously observed for long-lived electron−hole pairs generated by photoionization of biphenyl occluded in nonacidic M$_n$ZSM-5 (M = Li^+, Na^+, K^+, Rb^+, Cs^+). [26] In contrast, such absorption bands were never observed after photoionization of anthracene occluded in M$_n$ZSM-5. In this case, the electron−hole pair was not detected by EPR experiment and UV−visible absorption.

Photoionization of aromatic compounds in the condensed phase has been studied extensively in view of its importance in many areas of chemistry and physics. In nonpolar solvents immediately after ionization, a photoelectron ejected from NAP scatters on a continuous medium and becomes thermalized within a certain distance from NAP$^{\bullet+}$ often much smaller than the average Onsager radius**.** Thus, the majority of the electrons geminately recombines with NAP$^{\bullet+}$ within several picoseconds at room temperature, while the remainder escapes and homogeneously recombines with NAP$^{\bullet+}$ more slowly. In the same way in the case of polar solvents, an ionizing event can be characterized by the production of a NAP$^{\bullet+}$−electron pair. Then surrounding solvent molecules respond to the instantaneous charge creation. Vibrational relaxation as well as structural relaxation can occur in the time range of picoseconds, resulting in the generation of the solvated-free ions with lifetimes of several nanoseconds. If the initial cation−electron distance is shorter than the Onsager radius, then geminate recombination should compete with the formation of the solvated free ion.[7] In micellar media, it is interesting that the micelles induced retardation of the NAP$^{\bullet+}$−electron compact ion pair recombination. The Coulombic interactions were invoked to explain this feature.[8] Several papers have dealt with the photolysis and radiolysis of NAP included in the cavity network of X and Y faujasitic and aluminum-poor ZSM-5 zeolites.[3,4,9,10,11] A significant distinction between radiolysis and photolysis is the mode of energy absorption.[5] While radiolysis causes the ionization of the inorganic matrix and subsequent transfer to the guest, the photolysis involves resonant excitation of select molecules. The photoionization of NAP occluded at low loading in faujasitic Na_{51}Y (Si/Al ≈ 2.75) and Na_{85}X (Si/Al ≈ 1.32) zeolites generates NAP$^{\bullet+}$−electron pairs with lifetime on the order of several μs.[9,10] The high aluminum content and the numerous Na^+ extraframework of the faujasitic zeolites do not hinder efficiently the recombination of NAP$^{\bullet+}$ with the electron trapped as $Na_n^{(n-1)+}$ moieties in the supercages.[9,10] The relatively

(52) Marquis, S.; Moissette, A.; Vezin, H.; Brémard, C. *J. Phys. Chem. B* **2005**, *109*, 3723−3726.
(53) Moissette, A.; Vezin, H.; Gener, I.; Patarin, J.; Bremard, C. *Angew. Chem., Int. Ed*. **2002**, *41*, 1241−1244.
(54) Sahoo, R.; Debnath, R. *Adv. Mater.* **2003**, *15*, 287−289.

large diameter of the super cage (1.3 nm) was invoked to explain why the mobility of NAP species in the porous void space is not drastically reduced. It is probable that analogous behaviors were expected with other alkali metal cations as previously observed after the fast laser photolysis of biphenyl occluded in $M_{56}Y$ and $M_{85}X$ zeolites ($M = Na^+$, K^+, Cs^+).[55,56] The tight fit between the rod-shaped sorbate and the pore size of ZSM-5 zeolites was found to drastically reduce the mobility of occluded species within the channels.[19] However, the confinement effect of NAP within the channel of purely siliceous silicalite-1 was not found to be sufficient to slow efficiently the recombination of photoinduced $NAP^{\bullet+}$−electron pairs. The photolysis at 266 nm of NAP occluded in silicalite-1 was found not to generate any species durable enough at room temperature to be detected by conventional spectroscopic tools 2 min after the irradiation was stopped. Nevertheless, the X-ray or UV photolysis of NAP occluded in aluminum-poor ZSM-5 was reported previously to generate $NAP^{\bullet+}$ stable enough at 77 K to be studied by CW-EPR, ENDOR, and ESEEM spectroscopy.[11] The higher aluminum content of $M_{6.6}$ZSM-5 was found to dramatically increase the $NAP^{\bullet+}$ lifetime after photolysis of occluded NAP. The nature of alkali metal cation M^+ was found to be an important factor of the long life of the radical cation−electron pair. Analogous trends were previously reported during the photolysis of biphenyl occluded in M_nZSM-5.[39,57] Particularly, the combined effects of the tight fit of the biphenyl size and the ZSM-5 straight channel dimension, the high aluminum content, and the highly polarizing cation Li^+ increase dramatically the lifetime of the radical cation−electron pair in $Li_{6.6}$ZSM-5. The lifetime of this primary short distance charge separation state permits the use of the oxidizing power of the electron-deficient radical cation to capture an electron of the zeolite framework to create a long-lived electron−hole pair at room temperature.[39]

The very long lifetime of electron−hole pair NAP@$Li_{6.6}$ZSM-$5^{\bullet-\bullet+}$ exceeds several weeks at room temperature with high yield and has allowed the study of the charge separation distance and the atomic environment of the unpaired electrons using EPR measurements. The photoinduced charge separation proceeds via a sequence of ion-radical (electron−hole) pair states. The sequence is initiated when an electron leaves the photoexcited primary NAP donor and is transferred to trapping site in the vicinity of the Al(III) framework atom and extraframework Li^+ cation. The stability of the charge-separated state is facilitated by charge carrier delocalization through electron abstraction by the electron-deficient $NAP^{\bullet+}$ from electron-donating oxygen probably in the vicinity of the surrounding Al atom. The distance values between the electron and hole of the long-lived spin-correlated NAP@$M_{6.6}$ZSM-$5^{\bullet+\bullet-}$ pairs were found to be close to 1.3 nm and can correspond to Al- - -Al distance in the framework. The weak magnetic interactions between unpaired electrons and ^{27}Al, ^{29}Si, ^{7}Li, and ^{1}H nuclei were found to be in agreement with close proximity of the trapped electron with naphthalene facially coordinated to the Li^+ cation. The positive hole can be assumed to be located on the oxygen atom of another Si−O−Al bridge at a distance of 1.3 nm from the trapped electron. The electron-transfer rate for charge recombination of a very long-lived electron−hole pair in zeolites can be described by the Marcus theory.[46,58] The very low recombination rate by tunneling effect was found to be in reasonable agreement with the very low value ($J \approx 0$) of the magnetic exchange. It was reported recently that the majority of the charge separations lie in the normal region and most of the charge recombinations are in the inverted region.[58] The high electrostatic field on the range of several volts per ampere derived by the presence of Al(III) and small cations such as Li^+ in the narrow channel of ZSM-5. It is invoked to explain the unusual stability of the electron−hole pair generated by photoinduced injection of electron from NAP into the conduction band and generation of positive hole by $NAP^{\bullet+}$ electron abstraction in the valence band of the $Li_{6.6}$ZSM-5 zeolite.

Acknowledgment. The Centre d'Etudes et de Recherches Lasers et Applications (CERLA, FR-CNRS 2416) is supported by the Ministère chargé de la recherche, the région Nord/Pas de Calais, and the Fonds Européen de Développement Economique des Régions.

JA0518225

(55) Gener, I. Ph.D. Thesis, University of Lille, France, 1999.
(56) Gener, I.; Buntinx, G.; Moissette, A.; Brémard, C. *J. Phys. Chem. B* **2002,** *106*, 10322−10329.
(57) Gener, I.; Buntinx G.; Brémard C. *Angew. Chem., Int. Ed.* **1999**, *38*, 1819−1822.
(58) Zhang, G.; Thomas, J. K. *J. Phys. Chem. B* **2003**, *107*, 7254−7260.